Supplementary Information for: Large-scale experimental validation of thermochemical water-splitting oxides discovered by defect graph neural networks

Tyra C. Douglas[a,‡], Michael J. Dzara[b,‡], Andrew J. E. Rowberg[c], Keith A. King[d], Maria Syrigou[d], Nicholas A. Strange[e], Robert T. Bell[b], Anuj Goyal[b,f], Pin-Wen Guan[d], Robert B. Wexler[g], Joel B. Varley[c], Tadashi Ogitsu[c], Stephan Lany[b], Anthony H. McDaniel[d], Sean R. Bishop[a,*], and Matthew D. Witman[d,*]

[a] Sandia National Laboratories Albuquerque, NM 87123, USA

[b] National Renewable Energy Laboratory, Golden, CO 80401, USA

[c] Lawrence Livermore National Laboratory, Livermore, CA 94550, USA

[d] Sandia National Laboratories Livermore, CA 94550, USA

[e] Stanford Synchrotron Radiation Lightsource, SLAC National Accelerator Laboratory, Menlo Park, CA, 94025, USA

[f] Department of Materials Science and Metallurgical Engineering, IIT Hyderabad, Kandi, Sangareddy, Telangana 502284, India

[g] Department of Chemistry and Institute of Materials Science and Engineering, Washington University in St. Louis, St. Louis, MO 63130, USA

[‡] Equal contributions

[*] mwitman@sandia.gov ; srbisho@sandia.gov

Supplementary Section 1. DFT details

We conduct first-principles calculations based on density functional theory (DFT)[1,2] as implemented in the Vienna *Ab initio* Simulation Package (VASP).[3] Total energies are converged to within 10^{-6} eV, and forces were considered converged when below 10 meV/Å. Spin polarization was used for all calculations, and the lowest-energy spin configurations were systematically determined for compounds containing first-row transition metals. The specific pseudopotentials were chosen to correspond to standard selections for fitted elemental-phase reference energies (FERE), which in turn correct for standard deviations between DFT calculated and experimentally measured oxide enthalpies of formation.[4,5]

Additional training data calculations. Neutral vacancy formation energies in binary oxides of {Cr, Sn, Pr, Ga, Gd, Cs, Rb, Eu, Li, Na, K, Zn, Cd, Mo, W, Ta}, along with a handful of ternary compounds, were computed in this work to augment the dataset from our previous work [6]. The generalized gradient approximation of Perdew, Burke, and Ernzerhof (PBE-GGA)[7] was used for DFT exchange and correlation, along with a Hubbard U correction term.[5,8] All calculations involve a 380 eV energy cutoff, in conjunction with the soft O_s PAW dataset. A gamma-centered k-point mesh with a density of 1,000 points per reciprocal atom is chosen for all defect calculations. Besides its computational efficiency, the GGA+U functional allows us to utilize FERE,[4,5] which systematically improves the thermochemical properties in DFT calculations, including both the defect formation energies and the compound

formation enthalpies. The VASP projector augmented wave (PAW) pseudopotentials[9,10] and their version, U parameters, and reference chemical potentials ($\mu_X^{ref} = \mu_X^{FERE}$) for elements not included in our previous work[6] are shown in Supplementary Table 1. The training data needed to reproduce the model are provided in the accompanying supplementary data file "training_data.zip".

Supplementary Table 1: Pseudopotentials, version, U parameters, and reference chemical potentials used in this work to compute vacancy defect formation enthalpies.

VASP PP	Version	Ud	Uf	μ^{FERE}	$\mu^{HSE}_{\alpha=0.27}$	$\mu^{HSE}_{\alpha=0.3}$	$\mu^{HSE}_{\alpha=0.32}$
O_s	4.6			-4.76	-8.21	-8.56	-8.79
Li_sv	4.6			-1.65			
Na_pv	4.6			-1.06			
K_sv	4.6			-0.80			
Rb_sv	4.6			-0.68			
Cs_sv	4.6			-0.64			
Ca_pv	4.6			-1.64	-2.06		
Sr_sv	4.6			-1.17			-2.28
Ba_sv	4.6			-1.39		-2.23	
Mn	4.6	3.0		-7.00			
Cr_pv	4.6	3.0		-7.72			
Nb_pv	4.6	3.0		-6.69			
Ta_pv	4.6	3.0		-8.82			
W_pv	4.6	3.0		-10.06			
Mo_pv	4.6	3.0		-7.62			
Zn	4.6	6.0		-0.50			
Cd	4.6			-0.56			
Ga_d	4.6			-2.37	-3.92	-4.03	-4.10
In_d	4.6			-2.31	-3.54	-3.63	-3.70
Sn_d	4.6			-3.79			
Pr	5.4	1.5	2.0	-5.46			
Eu	5.4	1.5	2.0	-8.09			
Gd	5.4	1.5	2.0	-13.00			

Host supercells are relaxed with DFT in the ferromagnetic and different possible anti-ferromagnetic spin configurations. In the majority of cases, anti-ferromagnetic configurations are found to be lowest in energy. We chose anti-ferromagnetic configurations as an approximation for the high-temperature paramagnetic phase, as done in previous studies on vacancies in transition metal oxides.[6] The oxidation states of the transition metals and lanthanides are inferred from their calculated magnetic moment while maintaining the overall charge neutrality of a compound. For the defect calculations, larger host supercells are created, and depending on the space group symmetry, sizes between 64 and 540 atoms and shapes as close to cubic as possible are chosen such that periodic defect images are well separated from each other. For all materials, the minimum periodic image distance divided by the cube root of the supercell volume is between 0.82 and 1.12. Vacancies are created at all unique Wyckoff sites in the supercell. DFT energy minimization is performed involving only atomic position relaxations after randomly displacing the atoms (within 0.1 Å) around a vacancy site to break the local symmetry of the host. Forces in the defect calculations are converged within 2 meV Å^{-1}, and occupancies for the electronic states are determined using Gaussian smearing with a width of 0.05 eV. The automated workflow for vacancy formation enthalpies is the same as the reference.[6]

Our augmented dataset represents neutral oxygen and cation vacancy formation energies that combine training and validation data from [6], the dataset of [11], and the additional compounds in Supplementary Table 2. Supplementary Table 2 summarizes the composition, ID in NRELMatDb, ID in ICSD (if applicable), space group (SG), space group number (SG#), number of atoms in the unit cell (N_{UC}), multiplicity m of the supercell, and minimum periodic image distance divided by the cube root of the supercell volume ($d_{min}/\sqrt[3]{m \cdot V_{UC}}$).

Supplementary Table 2: Summary of additional training compounds added in this work.

Composition	NRELMatDb	ICSD	SG	SG#	N_{UC}	m	$d_{\mathrm{min}}/\sqrt[3]{m \cdot V_{\mathrm{UC}}}$
Cs2O1		27919	R-3m	166	3	32	1.09
Eu1O1		631466	Fm-3m	225	8	27	0.99
Gd1O1		24981	F-43m	216	8	27	0.99
Gd2O3		162247	P-3m1	164	5	32	0.9
Gd2O3		184528	C2/m	12	15	16	0.94
O1Rb2		77676	Fm-3m	225	3	32	1
O3W1	287089		Pbca	61	32	8	0.99
Cd1O1	9515		F-43m	216	2	32	1
K2O1	110305		Fm-3m	225	3	32	1
Mo1O3	165241		P2_1/c	14	32	8	0.99
O5Ta2	285203		Cm	8	14	16	0.99
O1Zn1	9402		P6_3mc	186	4	32	1.06
Mo4O11	180322		Pnma	62	60	9	0.82
Na2O1	290084		Fm-3m	225	3	32	1
Mo1O2	148078		P4_2/mnm	136	12	8	0.92
Li2O1	286994		Fm-3m	225	3	32	1
Cr2O3	9686	626479	R-3c	167	10	8	1.08
Ga2O3	9751	27431	R-3c	167	10	8	1.08
Ga2O3	9871	83645	C2/m	12	10	16	1.02
O2Sn1	10063	56671	P4_2/mnm	136	6	12	0.99
Nb2O5	290102		C2/c	15	14	4	0.89
Nb1O2	129259		C2/m	12	24	4	0.93
O1Sn1	10055	15516	P4/nmm	129	4	18	0.91
Pr1O2		105541	Cmce	64	12	8	0.99
Pr2O3		184533	Ia-3	206	40	2	0.99
Ba1Nb2O6	133995	39272	Pbam	55	18	6	0.91
Ca2Nb2O7	289796	26010	P2_1	4	44	4	0.83
Cr2Mg1O4	9565	160954	I4_1/amd	141	14	16	0.89
Mg1Nb2O6	144307	85008	Pbcn	60	36	4	0.86
Nb2O7Sr2	129363	187	Cmc2_1	36	22	6	0.92
Nb2O9Sr4	182299	79217	P6_3/m	176	30	4	0.95
Nb2O6Sn1	165320	163815	C2/c	15	18	4	0.91
Cr2O8Sr3	138915	85055	C2/m	12	13	4	1.03
Cr1O4Sr1	156232	160793	P2_1/c	14	24	4	1.01
Cr1O4Sr2	171839	26944	Pna2_1	33	56	2	0.85
Nb1O3Sr1	165001	88723	P2_1/c	14	20	8	0.88
Ba1Pr1O3		163752	Pnma	62	20	4	1.12
Ba1Pr1O3		163755	Pm-3m	221	20	2	0.99
Pr1Mn1O3		97081	Pnma	62	20	8	0.88
Pr1Mn2O5		84669	Pbam	55	32	2	0.83

{Ca,Sr,Ba}{Ga,In}$_4$O$_7$ and Sr$_3$PrMn$_2$O$_8$ calculations. Additional DFT validation was performed on dGNN screening predictions for MP structures containing less-represented cations (Pr, Ga) in the training data. We use an energy cutoff of 360 eV for the PAW plane-wave basis set, with the pseudopotentials as listed in Supplementary Table 1.[9,10] For compounds with a band gap (here, {Ca,Sr,Ba}{Ga,In}$_4$O$_7$), the hybrid exchange-correlation functional of Heyd, Scuseria, and Ernzerhof (HSE06) was used,[12,13] as it provides superior accuracy for electronic properties in semiconductors and insulators.[14] The fraction of exact exchange, α, used in the hybrid functional was set to match experimentally measured band gaps as closely as possible.

For both {Ca,Sr,Ba}{Ga,In}$_4$O$_7$ and Sr$_3$PrMn$_2$O$_8$, we also applied PBE-GGA using the U corrections described in Supplementary Table 1. Formation energies of oxygen vacancies (V_{O}) are calculated using supercells. For {Ca,Sr,Ba}{Ga,In}$_4$O$_7$, supercells were constructed by doubling the unit cells along the **b** and **c** axes, resulting in cells with 192 atoms. For Sr$_3$PrMn$_2$O$_8$, supercells are constructed by doubling the size of the unit cell along the **a** and **b** directions, resulting in a simulation cell with 112 atoms. In each case, relaxations were performed with a

single **k** point at Γ.

For {Ca,Sr,Ba}{Ga,In}$_4$O$_7$, containing 48 atoms per monoclinic unit cell (space group $C2/c$), a $1 \times 2 \times 3$ Γ-centered **k**-point grid was used to relax the unit cell. For $Sr_3PrMn_2O_8$, containing 28 atoms in its orthorhombic unit cell (space group $Amm2$), we use a Γ-centered $8 \times 8 \times 2$ **k**-point mesh to relax the unit cell. We find that the ground-state spin configuration is ferromagnetic on the Pr sublattice and antiferromagnetic on the Mn sublattice, with net spin moments of $2.0\mu_B$ and $\pm 3.3\mu_B$ for Pr and Mn, respectively, and an overall moment of $3.9\mu_B$ per unit cell. Unit cell dimensions and band gaps for each of these materials are listed in Supplementary Table 3, and compared to experiment where possible.

Supplementary Section 2. DFT re-validation of {Pr,Ga,In}-containing compounds.

Additional details of the HSE and PBE-GGA calculations for {Ca,Sr,Ba}{Ga,In}$_4$O$_7$ and $Sr_3PrMn_2O_8$ are shown in Supplementary Table 3, including errors with respect to experimentally determined unit cell dimensions and band gaps, where available. Note that, for $Sr_3PrMn_2O_8$, we compare to an experimental structure containing 50% Cr substitution for Mn.[15]

PBE-GGA systematically under-predicts the HSE-computed min(ΔH_{V_O}) by ∼0.5 eV for {Ca,Sr,Ba}{Ga,In}$_4$O$_7$ compounds. This has substantial implications for the true positive/false positive (TP/FP) classification, namely that, with PBE-GGA, both {Sr,Ba}{Ga}$_4$O$_7$ satisfy our down-selection criteria of min(ΔH_{V_O}) < 4.0 eV, while with HSE they do not. The relatively large and systematic discrepancy can be rationalized as follows. Formation of V_O in Ga-containing compounds (as well as In-containing) involves bond formation between neighboring Ga p states and introduces a defect state particularly close to the valence band minimum (VBM). This differs from the typical observation in transition metal oxides, where the defect state is relatively deep within the band gap and therefore is less strongly affected by the choice of functional. Here, the change in energy can almost entirely be explained by the change in relative position between the defect state and band edge when moving from PBE to HSE, which improves the description of band edge and defect level positions. PBE also tends to underbind structures, which may allow Ga/In atoms to undergo inaccurately large displacements around the vacancy.

Supplementary Table 3: Calculated and experimental values of lattice parameters, band gaps, and neutral oxygen vacancy formation energies for materials relevant to this work.

Material	Method	a [Å]	b [Å]	c [Å]	E_g [eV]	min(ΔH_{V_O}) [eV]
$CaGa_4O_7$	HSE, $\alpha = 0.27$	13.10	9.14	5.62	4.69	4.17
	PBE-GGA	13.26	9.22	5.70	2.54	3.78
	Experimental	13.13[a]	9.12[a]	5.61[a]	4.68[b]	–
$SrGa_4O_7$	HSE, $\alpha = 0.32$	13.45	9.21	5.70	4.95	4.03
	PBE-GGA	13.65	9.32	5.78	2.43	3.59
	Experimental	13.7[c]	9.3[c]	5.8[c]	4.95[d]	–
$BaGa_4O_7$	HSE, $\alpha = 0.30$	13.66	9.42	5.79	4.66	3.91
	PBE-GGA	13.86	9.50	5.86	2.31	3.50
$CaIn_4O_7$	HSE, $\alpha = 0.27$	13.97	10.06	6.05	3.22	2.94
	PBE-GGA	14.10	10.13	6.13	1.44	2.60
$SrIn_4O_7$	HSE, $\alpha = 0.32$	14.91	10.49	5.91	3.55	3.02
	PBE-GGA	14.44	10.20	6.20	1.51	1.49
$BaIn_4O_7$	HSE, $\alpha = 0.30$	14.99	10.40	6.14	3.45	2.38
	PBE-GGA	15.14	10.44	6.25	1.56	1.93
$Sr_3PrMn_2O_8$	PBE-GGA	5.51	5.51	12.40	–	2.62
$Sr_3PrMnCrO_8$	Experimental[f]	5.41	5.41	12.48	–	–

[a]Ref [16]; [b]Ref [17]; [c]Ref [18]; [d]Ref [19]; [e]This work; [f]Ref [15]

Supplementary Section 3. Full Formation Energies for Alkaline-Earth Gallium Oxides

As discussed in the main text, defects in materials with a band gap may have different charge states depending on the position of the Fermi level. The formation energy $E^f(D^q)$ of a defect D in charge state q can be calculated as a function of Fermi level position as follows:[20]

$$E^f(D^q) = E(D^q) - E_{\text{bulk}} + \sum n_{\text{A}}\mu_{\text{A}} + qE_F + \Delta_{\text{corr}}. \tag{1}$$

Here, $E(D^q)$ is the total energy of a supercell containing D^q; E_{bulk} is the total energy of the pristine, defect-free supercell; n_{A} is the number of atoms of species A added ($n_{\text{A}} < 0$) or removed ($n_{\text{A}} > 0$) to create the defect; μ_{A} is the chemical potential of A; E_F is the position of the Fermi level relative to the valence band maximum (VBM); and Δ_{corr} is a correction term for charged defects to account for spurious self-interactions across periodic boundaries.[21,22] Computing these correction energies requires knowledge of the dielectric tensor, which can be decomposed into ionic and electronic contributions. In Supplementary Table 4, we list the components of our computed dielectric tensors for {Ca,Sr,Ba}Ga4O7, the only materials for which we calculate charged defects in this work.

Supplementary Table 4: Calculated ionic and electronic components to the dielectric tensor for {Ca,Sr,Ba}Ga_4O_7, as computed with the HSE hybrid functional and a mixing parameter α selected to reproduce the experimental band gap.

	$CaGa_4O_7$ ($\alpha = 0.27$)					
	ε_{xx}	ε_{yy}	ε_{zz}	ε_{xy}	ε_{xz}	ε_{yz}
ionic	3.00	4.81	7.59	0.00	0.00	–1.44
electronic	2.71	2.67	2.75	0.00	0.00	0.00
total	5.72	7.48	10.35	0.00	0.00	–1.44
	$SrGa_4O_7$ ($\alpha = 0.32$)					
	ε_{xx}	ε_{yy}	ε_{zz}	ε_{xy}	ε_{xz}	ε_{yz}
ionic	3.91	5.02	7.18	0.00	0.00	–1.16
electronic	2.61	2.60	2.65	0.00	0.00	–0.02
total	6.52	7.72	9.83	0.00	0.00	–1.17
	$BaGa_4O_7$ ($\alpha = 0.30$)					
	ε_{xx}	ε_{yy}	ε_{zz}	ε_{xy}	ε_{xz}	ε_{yz}
ionic	3.33	4.44	5.64	0.00	0.00	0.01
electronic	2.72	2.69	2.73	0.00	0.00	–0.02
total	6.05	7.12	8.37	0.00	0.00	–0.01

The formation energy is related to the defect concentration c as:

$$c = N_{\text{sites}} \exp\left(-\frac{E^f}{k_B T}\right), \tag{2}$$

where N_{sites} is the site concentration of the defect, and k_B is Boltzmann's constant. Lower formation energies thus correspond to exponentially higher defect concentrations. Initially, E_F is treated as an independent variable in calculating formation energies, meaning that plots of E^f *vs.* E_F will show each defect as a line with slope q, with changes in slope corresponding to transitions in the thermodynamically preferred charge state. The actual position of E_F is subsequently determined by the position where the lines corresponding to the lowest energy positively and negatively charged defects intersect, or, in other words, where there are equal concentrations of positively and negatively charged defects, leading to overall charge neutrality.

The chemical potentials μ_{A} reflect the energetic preference for specific elements under chosen conditions. We define these values based on their deviation $\Delta\mu_{\text{A}}$ from a reference energy as:

$$\mu_{\text{A}} = E_{\text{A}} + \Delta\mu_{\text{A}}, \tag{3}$$

where E_A is the total energy of the elemental reference structure, specifically, fcc Ca and Sr, bcc Ba, base-centered orthorhombic Ga, bct In, and molecular O_2. Our use of the "soft" O_s pseudopotential leads to underbinding of the O_2 molecule, requiring a correction. Specifically, we define the elemental O_2 energy as the sum of the energy of an O atom, computed using the O_s pseudopotential, and the molecular binding energy of the O_2 molecule as computed using the "hard" O_h pseudopotential from VASP version 4.6. This approach has been shown to yield accurate energies for the O_2 molecule while enabling continued use of the O_s pseudopotential in defect calculations,[23] which otherwise would be significantly more expensive. We compute reference energies for all species individually for each HSE mixing parameter α and list them in Supplementary Table 1. To facilitate direct comparison between PBE and HSE results, we do not use a FERE-corrected value for μ_O, but instead use a value of -5.04 eV, computed using this same approach. We use this value for calculations of $Sr_3PrMn_2O_8$, as well as for $\{Ca,Sr,Ba\}\{Ga,In\}_4O_7$.

To prevent the precipitation of these elemental phases, $\Delta\mu_A \leq 0$ for each element A. We assume conditions corresponding to thermodynamic equilibrium, which can be expressed for $\{Ca,Sr,Ba\}Ga_4O_7$ as:

$$\Delta\mu_{Ca/Sr/Ba} + 4\Delta\mu_{Ga} + 7\Delta\mu_O = \Delta H^f(\{Ca/Sr/Ba\}Ga_4O_7), \tag{4}$$

where $\Delta H^f(\{Ca/Sr/Ba\}Ga_4O_7)$ is the enthalpy of formation, based on reference energies computed with tabulated fitted elemental-phase reference energies (FERE).[4] Further bounds are enforced by prohibiting the precipitation of secondary phases:

$$a\Delta\mu_{Ca/Sr/Ba} + b\Delta\mu_{Ga} + c\Delta\mu_O \leq \Delta H^f(\{Ca/Sr/Ba\}_a Ga_b O_c). \tag{5}$$

Possible limiting phases and their formation enthalpies are identified through the National Renewable Energy Laboratory's Computational Materials Science Materials Database (`https://materials.nrel.gov/`).[4]

We can explore variations in chemical environments within the regions of stability, shown for $\{Ca,Sr,Ba\}Ga_4O_7$ in Fig. 1 (a)-(c) and for $\{Ca,Sr,Ba\}In_4O_7$ in panels (d)-(f). As we discuss in the main text, none of the $\{Ca,Sr,Ba\}In_4O_7$ are thermodynamically stable; at all chemical potential conditions, a combination of secondary phases will be thermodynamically favored. For the $\{Ca,Sr,Ba\}Ga_4O_7$ compounds, we focus on conditions where $\Delta\mu_O = -2.5$ eV, corresponding to typical conditions for thermochemical hydrogen (TCH) production. At this value, there is a narrow range of $\Delta\mu_{\{Ca,Sr,Ba\}}$ and $\Delta\mu_{Ga}$ for which stability is maintained. Conditions for which $\Delta\mu_{\{Ca,Sr,Ba\}}$ is maximized are denoted as "{Ca,Sr,Ba}-rich;" these correspond to the onset of precipitation of $CaGa_2O_4$, $SrGa_2O_4$, or $Ba_4Ga_2O_7$. Similarly, $\Delta\mu_{Ga}$ is maximized at "Ga-rich" conditions, where the precipitation of Ga_2O_3 becomes thermodynamically favorable. We also refer to intermediate conditions between these two limits.

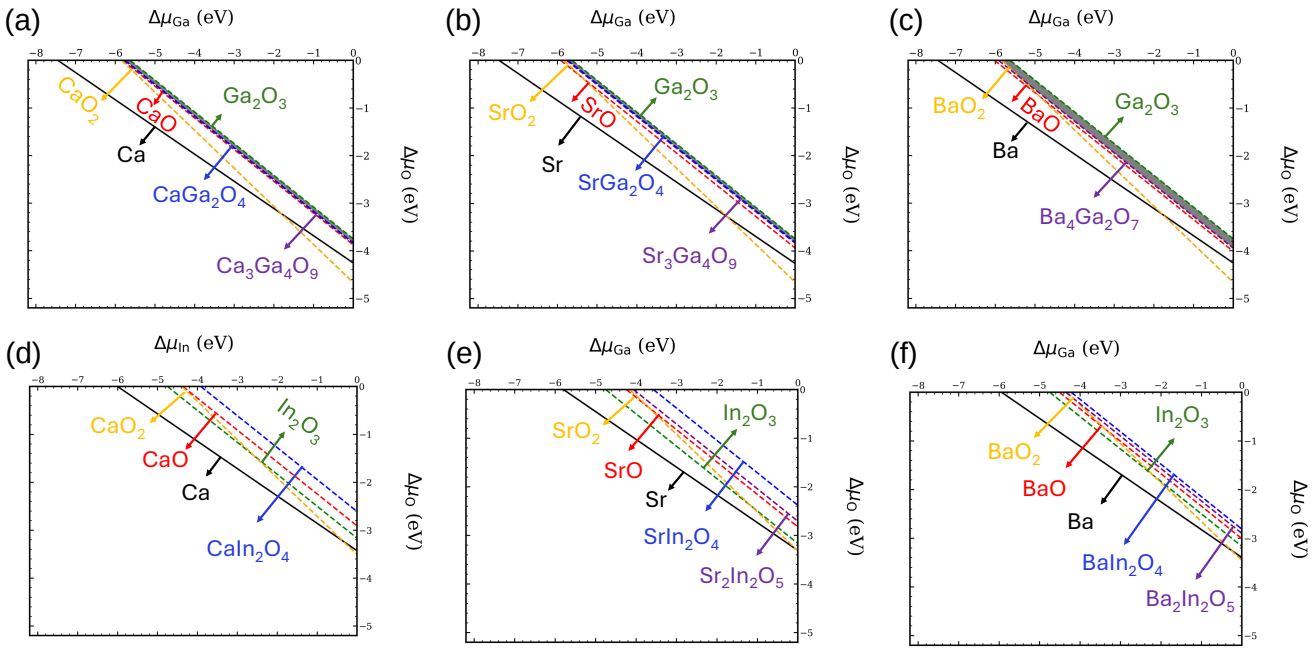

Supplementary Figure 1: Chemical potential stability regions (shaded in gray) for (a) $CaGa_4O_7$, (b) $SrGa_4O_7$, (c) $BaGa_4O_7$, (d) $CaIn_4O_7$, (e) $SrIn_4O_7$, and (f) $BaIn_4O_7$.

Defect formation energies are plotted in Fig. 2 for each of these three conditions in $CaGa_4O_7$ (panels a-to-c),

$SrGa_4O_7$ (panels d-to-f), and $BaGa_4O_7$ (panels g-to-i). Vacancies (V_A), interstitials (A_i), and cation antisites (A_B) are explicitly considered, capturing the most probable native point defects. The expected position of the Fermi level, E_F, is labeled with a dashed black line based on where equal concentrations of positively and negatively charged defects are expected. Notably, for each material and each condition, at this equilibrium Fermi level position, the lowest-energy charge state for oxygen vacancies will be neutral, which follows from the slope of the V_O formation energy line being zero at that position. As such, our reported values for the formation energy of V_O^0 are likely to be representative of true oxygen vacancy formation energies in undoped materials. The transition between the +2 and 0 charge states occurs 2.29 eV above the VBM in $CaGa_4O_7$, 2.36 eV above the VBM in $SrGa_4O_7$, and 2.16 eV above the VBM in $BaGa_4O_7$. The +1 charge state, depicted in the formation energy diagrams with a dashed blue line, will not be thermodynamically favored at any Fermi level position, although it may be present as a minority species. In $CaGa_4O_7$, charge neutrality will be established by equal concentrations of cation antisite defects, Ga_{Ca}^{+} and Ca_{Ga}^{-}. In $SrGa_4O_7$, depending on the chemical potential conditions, the lowest-energy donor defects will be Sr_i^{2+} or Ga_{Sr}^{+}, and the lowest-energy acceptor defect will be O_i^{-}. Finally, in $BaGa_4O_7$, the lowest-energy donor defects will be Ba_i^{2+} or V_O^{+}, and the lowest-energy acceptor defect will be O_i^{-}. While we have not calculated complete defect formation energies in the In-containing analogues, the general trends are similar, particularly as relates to V_O.

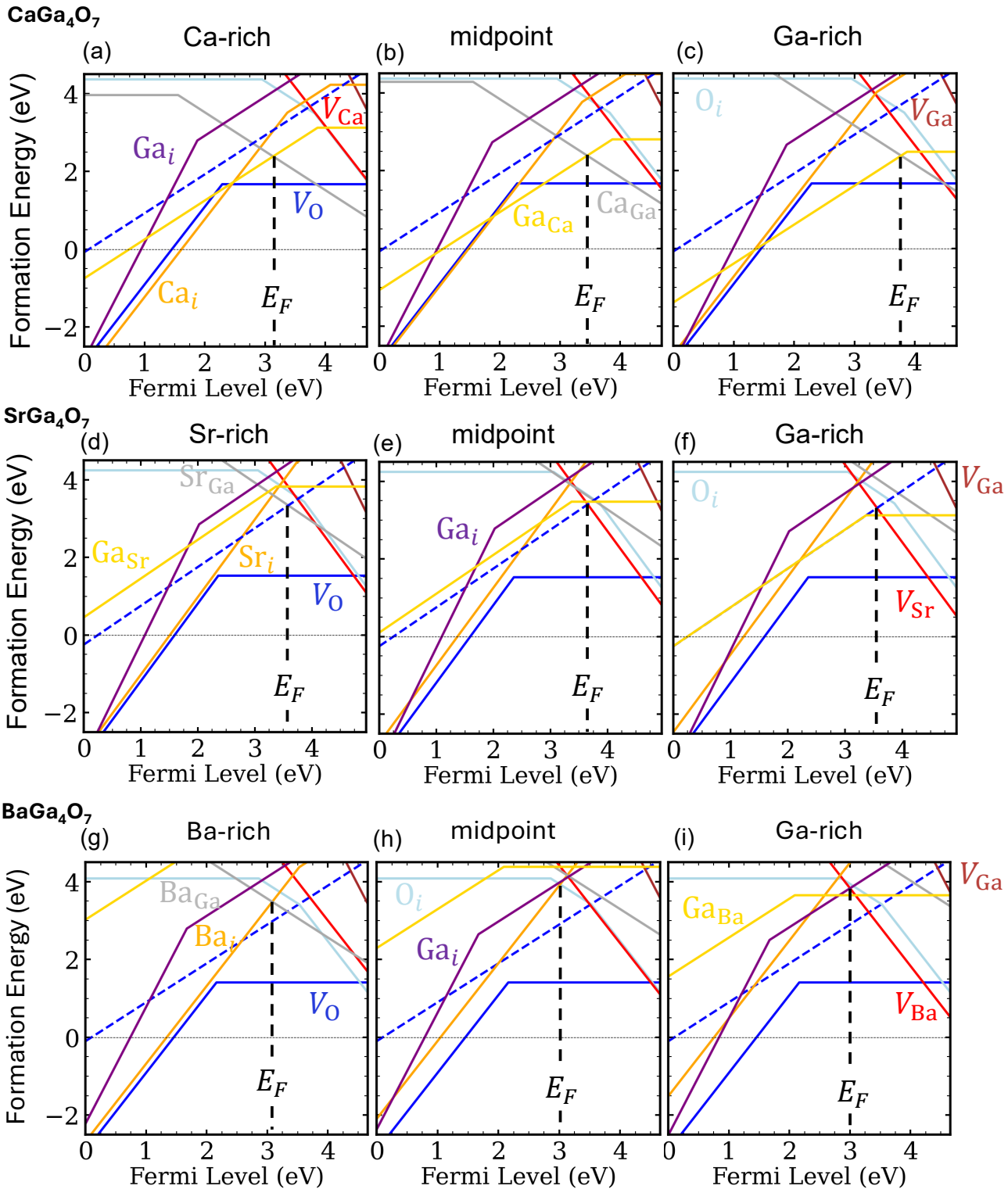

Supplementary Figure 2: Defect formation energies in $CaGa_4O_7$ under (a) Ca-rich, (b) intermediate, and (c) Ga-rich chemical potential conditions; defect formation energies in $SrGa_4O_7$ under (d) Sr-rich, (e) intermediate, and (f) Ga-rich chemical potential conditions; and defect formation energies in $BaGa_4O_7$ under (g) Ba-rich, (h) intermediate, and (i) Ga-rich chemical potential conditions.

Supplementary Section 4. dGNN model details

Automating predictions of relaxed defect structure properties from a host crystal structure is composed of several major steps. The key difference with dGNN compared to a typical GNN used for global property prediction (energy, band gap, bulk modulus etc.) is that, instead of a global pooling of all node features to derive a singular feature vector from which the final property prediction is derived, we extract the final prediction from the post-convolution feature vector corresponding to the vacancy site, i, in the host structure. The dGNN architecture in this work closely mimics that of CGCNN, because it is readily amenable to a simple architecture with low parameter complexity (needed for our small dataset). In principle, more advanced equivariant GNN architectures could be explored in the future, but previous tests showed no improvement and greater propensity for over-fitting, likely due to the very small size of our training dataset ($< 2,000$ vacancy formation energies). The details of the model architecture are as follows:

1. The relaxed *host* crystal structure $\mathcal{C}_\langle$ is constructed as a graph with nodes corresponding to atoms and edges representing connections between neighboring atoms with distance less than a cutoff radius, $r_c = 5.0$ Å.

2. The initial node feature vector of atomic site i, $\boldsymbol{v}_i^{(t=0)}$, is generated by one-hot encoding its atomic number. Initial edge features between neighbors i and j, $\boldsymbol{b}_{ij}$, are encoded by two-body symmetry functions[24] of the bond distance according to a set of Gaussian widths (η), centers (R_s), r_c, and a cutoff function, f_c:

$$\boldsymbol{b}_{ij} = \{\exp\left[-\eta(r_{ij} - R_s)^2\right] f_c(r_{ij})\}. \tag{6}$$

   Here we use $\eta = \{0.5, 1.0, 1.5\}$, $R_s = \{1.0, 2.0, 3.0, 4.0, 5.0\}$, and

$$f_c(r_{ij}) = \begin{cases} \left(\cos\left(\dfrac{\pi r_{ij}}{r_c}\right) + 1\right)/2 & \text{for } r_{ij} \leq r_c \\ 0 & \text{for } r_{ij} > r_c \end{cases} \tag{7}$$

3. At each convolution layer, t, node feature vectors are updated according to the following filter:

$$\boldsymbol{v}_i^{(t+1)} = g\left(\boldsymbol{v}_i^{(t)} + \sum_j \sigma\left(\boldsymbol{z}_{ij}^{(t)}\boldsymbol{W}_1^{(t)} + \boldsymbol{b}_1^{(t)}\right) \odot g\left(\boldsymbol{z}_{ij}^{(t)}\boldsymbol{W}_2^{(t)} + \boldsymbol{b}_2^{(t)}\right)\right). \tag{8}$$

   Here $\boldsymbol{z}_{ij} = \boldsymbol{v}_i \oplus \boldsymbol{v}_j \oplus \boldsymbol{b}_{ij}$ is the concatenation of features between connected nodes in the graph, $\boldsymbol{W}_1$,$\boldsymbol{W}_2$ and b_1, b_2 represent weights and biases of different learnable weight matrices (i.e., fully connected neural network layers), σ denotes a sigmoid activation function, g denotes a softplus activation, and $\odot$ denotes element-wise multiplication.

4. Following t' convolution layers, the node feature vector corresponding to the crystallographic site index forming the vacancy, $\boldsymbol{v}_d = \boldsymbol{v}_i^{(t')}$.

5. Finally, n_h fully connected hidden layers are utilized to predict the relaxed vacancy formation enthalpy, using $\boldsymbol{v}_d$ as input.

All training data, model structures, and hyperparameters used in this study can be found in our Zenodo repository,[25] and the pre-trained models can be reproduced using our dGNN implementation[26] built in Pytorch[27] provided at `https://github.com/mwitman1/cgcnndefect/tree/Paper1` (a modified fork of CGCNN[28]). In brief, due to the small size of our training data set, a dGNN model of minimal complexity is required to facilitate training. In practice, the number of trainable parameters often exceeds the number of training examples in deep learning applications, and explicit regularization is not always needed to achieve low generalization error.[29] Nonetheless, our minimal complexity architecture consists of $T = 2$ convolution steps, $\boldsymbol{v}_i \in \mathbb{R}^8$, and $\boldsymbol{v}_d \in \mathbb{R}^{16}$, leading to a GNN with only $\sim 2,000$ learnable parameters. Consequently, the model is very computationally efficient. For example, utilizing just CPU execution of the pytorch-based model on an Apple M4 Max, inference of $\Delta H_{\mathrm{V_O}}$ for a batch of (all) sites corresponding to the 252 atom supercell for mp-19285 requires ~ 150 ms, which is shorter than the default command in the ASE package to read the structure into memory (~ 180 ms). After fixing the architecture, the learning rate was adjusted to minimize K-fold test set performance (next section), and over-fitting was minimized via early-stopping using the MAE on a 10% validation set within each train fold.

Supplementary Section 5. Cross-validation details

CV splits were generated using the MatFold code (`https://github.com/d2r2group/MatFold`). To evaluate the model performance, we denote the mean absolute error of an outer test set

$$\mathrm{MAE} = 1/N_k \sum_i |\widehat{\Delta H}_{\mathrm{V},i} - \Delta H_{\mathrm{V},i}|, \tag{9}$$

where N_k is the number of samples in outer fold k, $\widehat{\Delta H}_{\mathrm{V},i}$ is the model prediction of sample i, and $\Delta H_{\mathrm{V},i}$ the truth value. The expected model performance is given as the ensemble average over the set of all K folds,

$$\langle \mathrm{MAE} \rangle = \langle \{\mathrm{MAE}\}_K \rangle. \tag{10}$$

For non-nested CV, *i.e.*, K-fold, $\widehat{\Delta H}_{\mathrm{V},i}$ in the k^{th} test set is predicted by a single model trained on the k^{th} train set. For nested CV, *i.e.*, (K, L)-fold, the final prediction is the ensemble average over the set of inner model predictions on the outer test set,

$$\widehat{\Delta H}_{\mathrm{V},i} = \langle \{\widehat{\Delta H}_{\mathrm{V},i}\}_L \rangle. \tag{11}$$

The deviation of that ensemble average prediction from the true value is referred to as the residual or absolute error (AE), calculated as

$$\mathrm{AE} = \left| \Delta H_{\mathrm{V},i} - \langle \{\widehat{\Delta H}_{\mathrm{V},i}\}_L \rangle \right|. \tag{12}$$

Importantly, nested CV also yields an uncertainty metric via the standard deviation over the set of inner model predictions on the outer test set,

$$\sigma(\widehat{\Delta H}_{\mathrm{V},i}) = \sigma(\{\widehat{\Delta H}_{\mathrm{V},i}\}_L). \tag{13}$$

Supplementary Section 6. Material synthesis

Solid-state methods were used to synthesize each material. For $Ba_6La_2Fe_4O_{15}$, $Ba_5SrLa_2Fe_4O_{15}$, $Ba_3YFe_2O_{7.5}$, and $Ba_{2.5}Sr_{0.5}YFe_2O_{7.5}$, stoichiometric amounts of precursors designated by a "*" in Supplementary Table 5 were pretreated under the described conditions and weighed and subsequently ground by hand with an agate mortar and pestle. Samples were pressed into 1" dense pellets in a steel die under high vacuum ($< 1 \times 10^{-5}$ Torr) at 10 °C using an OxyGon hydraulic environment-controlled press. Force was ramped at a rate of 1,000 lbs/min to a maximum value of 20,000 lbs which was held for 15 minutes before ramping down to 1,000 lbs at the same rate. Sample pellets were then fired at 1050 °C in stagnant air in a Pt crucible for 20 hours, with 5 °C/min heating rates. Additional grind, press, and fire sequences were performed first at a firing temperature of 1300 °C, and then 3 more iterations with a firing temperature of 1500 °C were carried out.

All other materials were prepared using the remaining precursor powders (Supplementary Table 5) treated under the specified conditions. Stoichiometric amounts of powder were ball milled in water for 24 h, subsequently dried, and loaded into alumina crucibles for calcination under the conditions shown in Supplementary Table 6. A heating rate of 10 °C/min was used for each calcination. Some materials displayed irreversible mass change during the TGA screening due to particle size or morphology. These materials were pre-sintered by calcining 0.8 g, 6 mm diameter pellets in alumina crucibles lined with Pt foil and sacrificial powder. The pellets were crushed and sieved to 1mm – 250 μm for TGA analysis. Particle sizes < 250 μm were used for flow reactor measurements. Details on pre-sintered materials and conditions are also shown in Supplementary Table 6.

Supplementary Table 5: Precursor powders and pretreatment conditions used for material synthesis. Dashes indicate precursors that were used as received.

Precursor	Purity	Temp [°C]	Time [h]	Gas Used
$BaCO_3^*$	Sigma Aldrich (99.98%)	-	-	-
$SrCO_3^*$	Sigma Aldrich (99.9%)	-	-	-
$La_2O_3^*$	Sigma Aldrich (99.9%)	900	5	Room Air
$Y_2O_3^*$	Sigma Aldrich (99.99%)	-	-	-
$Fe_2O_3^*$	Sigma Aldrich (99.995%)	-	-	-
$BaCO_3$	Sigma Aldrich ($\geq$ 99%)	800	1	Room Air
$CaCO_3 \rightarrow CaO$	Thermo Scientific (99.5%)	900	1	Room Air
$SrCO_3$	Sigma Aldrich ($\geq$ 99%)	800	1	Room Air
Fe_2O_3	Thermo Scientific (99.9%)	800	1	Room Air
Pr_6O_{11}	Lindsay Chemical (Unknown)	450	3	Room Air
MoO_3	Alfa Aesar (%) (Unknown)	-	-	-
Co_3O_4	Sigma Aldrich ($71-74\%$)	-	-	-
$MoCaO_4$	Thermo Scientific (99%)	-	-	-
MnO_2	Sigma Aldrich ($\geq$ 99%)	600	1	Room Air

* Precursors used in the synthesis of $Ba_6La_2Fe_4O_{15}$, $Ba_5SrLa_2Fe_4O_{15}$, $Ba_3YFe_2O_{7.5}$, and $Ba_{2.5}Sr_{0.5}YFe_2O_{7.5}$

Supplementary Table 6: Solid State Synthesis Conditions.

Reaction	Calcination Temp. [°C]	Calcination Time [h]	Gas Used	Pre-sintered
$BaCO_3 + 2\ Fe_2O_3 \rightarrow BaFe_2O_4$	1400	4	Room Air	Y
$2\ BaCO_3 + Fe_2O_3 \rightarrow Ba_2Fe_2O_5$	1200	12	Ar	Y
$SrCO_3 + Pr_6O_{11} + MnO_2 \rightarrow Sr_{1.5}Pr_{0.5}MnO_4$	1400	3	Room Air	N
$BaCO_3 + Co_3O_4 + MoO_3 \rightarrow Ba_2CoMoO_6$	1100	1	H_2/Ar	Y
$Ba_2CoMoO_6 \rightarrow Ba_2CoMoO_6$	1100	3	H_2/Ar	Y
$BaCO_3 + BaMoO_4 \rightarrow Ba_2CaMoO_6$	1100	1	H_2/Ar	Y
$Ba_2CaMoO_6 \rightarrow Ba_2CaMoO_6$	1100	3	H_2/Ar	Y
$CaO + 2\ Ga_2O_3 \rightarrow CaGa_4O_7$	1300	6	Room Air	Y
$BaCO_3 + 2\ Ga_2O_3 \rightarrow BaGa_4O_7$	1300	3	Room Air	Y

Supplementary Section 7. XRD details and structural analysis

X-ray diffraction (XRD) was performed on as-synthesized and post-TGA cycled materials using beamline 2-1 at the Stanford Synchrotron Radiation Lightsource (SSRL) to confirm material purity and stability after testing. High-throughput sample manipulation, XRD measurements, and data processing were achieved using a robot-automated program described elsewhere.[30] Powders were loosely packed and sealed in 0.5 mm o.d. glass capillaries which were nested in 0.7 mm o.d. Kapton capillaries. Angle-dispersive measurements were performed at 17 keV between 2 and 113.5° (q $\sim$ 0.3 - 14.4 $Å^{-1}$) with a 1° step size and a $\sim$ 708 mm sample to detector distance. Data was acquired with a Pilatus 100K hybrid photon counting detector in a portrait orientation. 2D images were normalized, stitched, and integrated using a python script developed specifically for use a SSRL beamline 2-1. $TiNb_2O_7$ as-synthesized and post-TGA cycled samples were measured using a Bruker D6 diffractometer equipped with a LYNXEYE XE-T detector. The measurements were performed using Cu Kα radiation, a 0.02° step size, and 2 s exposure time. Phases were identified using CrystalDiffract[31] or Jade[32] and Rietveld refinements performed using TOPAS Academic, version 7.[33]

Identified major and secondary phases along with phase fractions are given in Supplementary Table 7. The intended phase for all materials were synthesized except $BaGa_4O_7$. This material was synthesized in the $I2/m$ structure, differing from the $C2/c$ structure provided by the Materials Project. We note that while the $I2/m$ structure does not appear in Materials Project, it is a calculated structure in the PDF Database.[34] $BaGa_4O_7$ contained several secondary phases including $BaGa_2O_4$ in the as-synthesized sample. However, unidentifiable phases inhibited phase fraction calculations. $TiNb_2O_7$, Ba_2CaMoO_6, Ba_2CoMoO_6, and $CaGa_4O_7$ as-synthesized and post-TGA cycled samples also contained small amounts of unidentifiable impurity phases. As-synthesized and post TGA cycled XRD patterns are shown in figures Supplementary Figure 3 and Supplementary Figure 4 for materials that exhibited reversible and irreversible mass change respectively.

Self-similar compounds $Ba_6La_2Fe_4O_{15}$, $Ba_5SrLa_2Fe_4O_{15}$, and $Ba_3YFe_2O_{7.5}$ were selected for study due to their intriguing structural motifs and potential flexibility for future compositional modification. Generally, Fe^{3+} is an attractive redox active cation, as demonstrated by the relative ease of reduction of Fe_2O_3 to Fe_3O_4 on an Ellingham diagram and its prevalence as the redox active cation in perovskites for TCH H_2 production. Within MP, each compound is predicted to crystallize in a monoclinic structure ($P2/c$), featuring octahedral coordinated La^{3+} or Y^{3+} and two unique Fe^{3+} sites. Fe^{3+} is tetrahedrally coordinated in both, with one site indicative of a single FeO_4 tetrahedron which corner shares with four equivalent LaO_6 or YO_6 octahedra. This structure has been confirmed experimentally for $Ba_3YFe_2O_{7.5}$.[35] The second Fe^{3+} site is an Fe_2O_7 tetrahedral dimer in which an apex oxygen anion is the linking site. This coordination environment has some similarity to the Mn_3O_{12} trimers which form within 12R-BCM,[36] making this family of monoclinic structures of interest for study as TCH water splitters. However, several studies that focused on magnetic structure and properties of $Ba_6La_2Fe_4O_{15}$ and $Ba_5SrLa_2Fe_4O_{15}$ have shown that these stoichiometries adopt a hexagonal symmetry ($P63mc$) in which the Fe^{3+} coordination adopts one FeO_6 octahedron and three FeO_4 tetrahedra per unit. These four Fe polyhedra are all corner sharing resulting in an Fe_4O_{15} cluster.[37] While $Ba_{2.5}Sr_{0.5}YFe_2O_{7.5}$ has not yet been reported and therefore was not included in the dGNN predictions, it was hypothesized to exist due to reports of its hexagonal La based analogue and therefore was also synthesized in this work to compare the impact of Sr A-site substitution in both materials. The intriguing nature and contrast in Fe coordination environments between such compositionally similar materials provides strong justification for study of this set of materials which has largely been unexplored at high temperatures.

Supplementary Table 7: Major and secondary phases identified in as-synthesized and Post-TGA cyled TCH Materials along with their phase fractions

Target Material	Phase Fraction (%)	
	Major Phase	Secondary Phase
$Ba_6La_2Fe_4O_{15}$ As-synthesized	$Ba_6La_2Fe_4O_{15}(P63mc)$	
	100	-
$Ba_6La_2Fe_4O_{15}$ Post-TGA	$Ba_6La_2Fe_4O_{15}(P63mc)$	
	100	-
$Ba_5SrLa_2Fe_4O_{15}$ As-synthesized	$Ba_5SrLa_2Fe_4O_{15}(P63mc)$	
	100	-
$Ba_5SrLa_2Fe_4O_{15}$ Post-TGA	$Ba_5SrLa_2Fe_4O_{15}(P63mc)$	
	100	-
$Ba_3YFe_2O_{7.5}$ As-synthesized	$Ba_3YFe_2O_{7.5}$ $(P2/c)$	-
	100	-
$Ba_3YFe_2O_{7.5}$ Post-TGA	$Ba_3YFe_2O_{7.5}$ $(P2/c)$	$Ba_3Y_{0.35}Fe_{0.65}O_{7.5}$ $(Pm\bar{3}m)$
	87.37	12.63
$Ba_{2.5}Sr_{0.5}YFe_2O_{7.5}$ As-synthesized	*$Ba_{2.5}Sr_{0.5}YFe_2O_{7.5}$ $(P2/c)$	$Ba_3Y_{0.35}Fe_{0.65}O_{7.5}$ $(Pm\bar{3}m)$
	81.69	18.31
$Ba_{2.5}Sr_{0.5}YFe_2O_{7.5}$ Post TGA	*$Ba_{2.5}Sr_{0.5}YFe_2O_{7.5}$ $(P2/c)$	$Ba_3Y_{0.35}Fe_{0.65}O_{7.5}$ $(Pm\bar{3}m)$
	54.89	2.57
$Sr_3PrMn_2O_8$ As-synthesized	$Sr_3PrMn_2O_8$ $(I4/mmm)$	
	100	-
$Sr_3PrMn_2O_8$ Post-TGA	$Sr_3PrMn_2O_8$ $(I4/mmm)$	
	100	-
$TiNb_2O_7$ As-synthesized	$TiNb_2O_7$ $(C2/m)$	Unknown
$TiNb_2O_7$ Post-TGA	$TiNb_2O_7$ $(C2/m)$	Unknown
$BaFe_2O_4$ As-synthesized	$BaFe_2O_4(Cmc2_1)$	-
	100	
$BaFe_2O_4$ Post-TGA	$BaFe_2O_4(Cmc2_1)$	-
	100	
$Ba_2Fe_2O_5$ As-synthesized	$Ba_2Fe_2O_5(P21/c)$	
	100	-
$Ba_2Fe_2O_5$ Post-TGA	$Ba_2Fe_2O_5(P21/c)$	$BaFe_2O_4(Cmc2_1)$
	97.65	2.35
Ba_2CaMoO_6 As-synthesized	Ba_2CaMoO_6 $(Fm\bar{3}m)$	Unknown
Ba_2CaMoO_6 Post-TGA	Ba_2CaMoO_6 $(Fm\bar{3}m)$	Unknown
Ba_2CoMoO_6 As-synthesized	Ba_2CoMoO_6 $(Fm\bar{3}m)$	Unknown
Ba_2CoMoO_6 Post-TGA	Ba_2CoMoO_6 $(Fm\bar{3}m)$	Unknown
$BaGa_4O_7$ As-synthesized	$BaGa_4O_7$ $(I2/m)$	$BaGa_2O_4$ $(P6_322)$
		Unknown
$BaGa_4O_7$ Post-TGA	$BaGa_4O_7$ $(I2/m)$	Unknown
$CaGa_4O_7$ As-synthesized	$CaGa_4O_7$ $(C2/c)$	Unknown
$CaGa_4O_7$ Post-TGA	$CaGa_4O_7$ $(C2/c)$	Unknown

* New structure templated by $Ba_3YFe_2O_{7.5}$ $(P2/c)$.

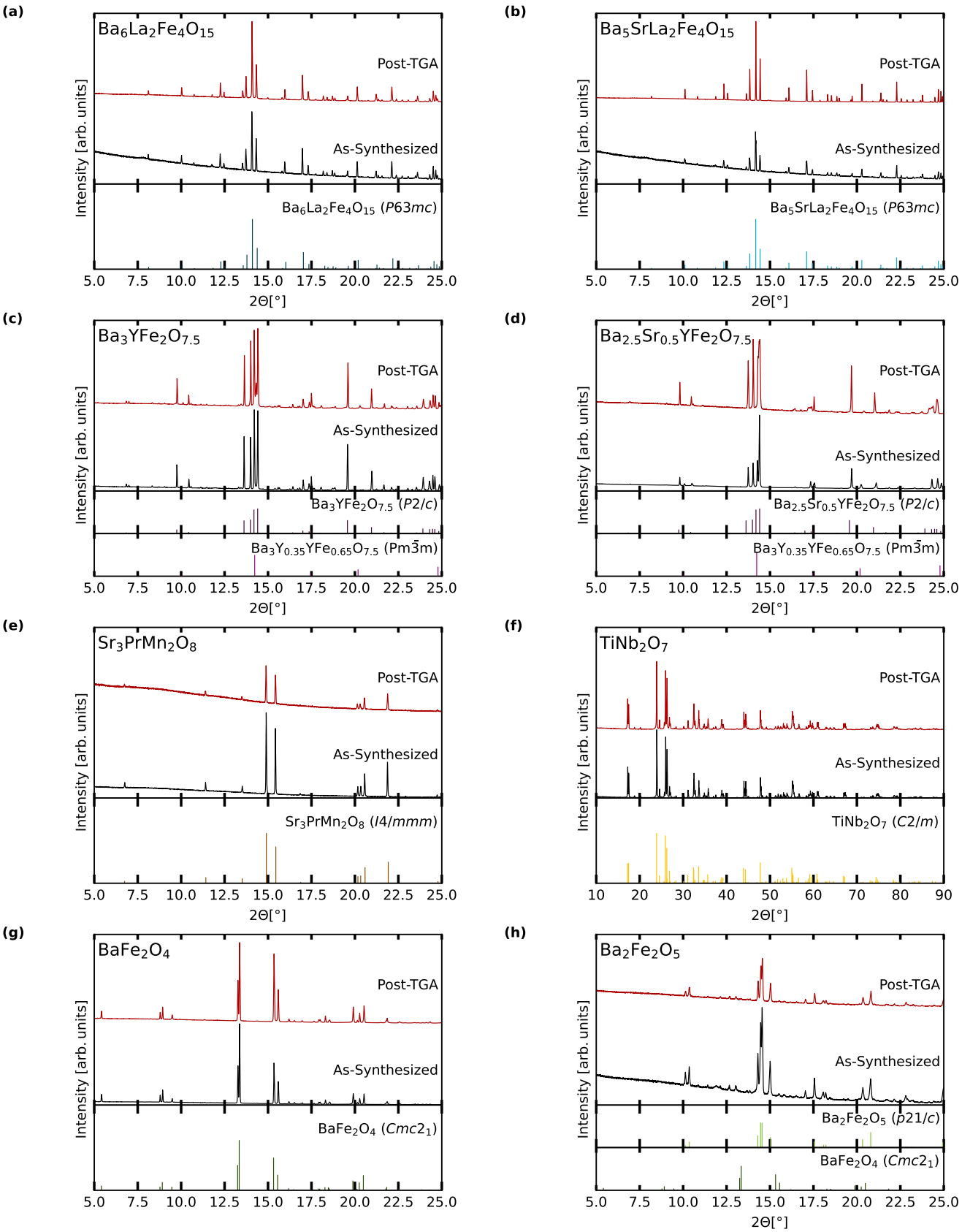

Supplementary Figure 3: As-synthesized and post-TGA XRD patterns of selected materials that exhibited reversible mass change in the TGA measurements.

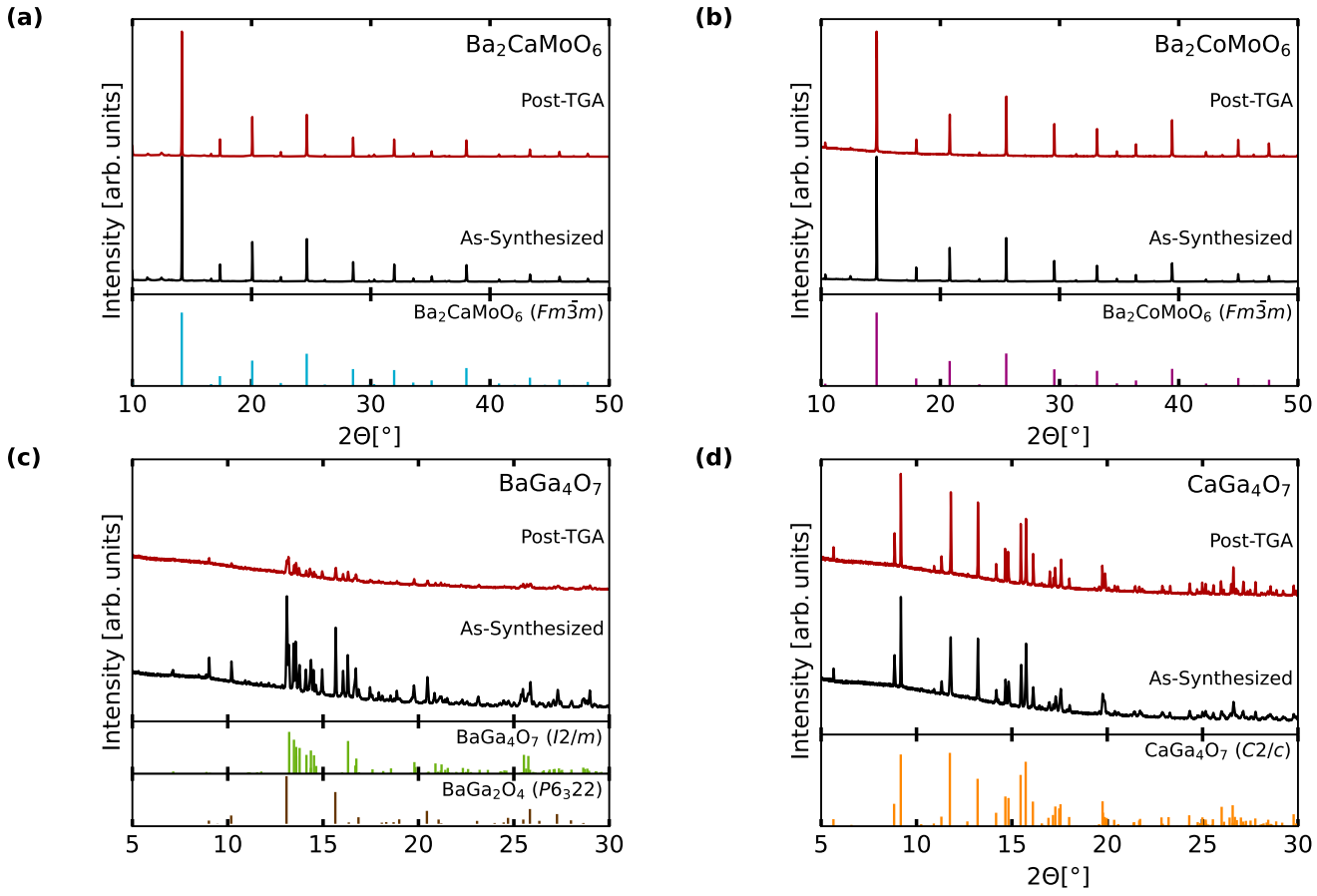

Supplementary Figure 4: As-synthesized and post-TGA XRD patterns of selected materials that exhibited irreversible mass change in the TGA measurements.

Supplementary Section 8. TGA redox cycles

TGA measurements were performed on Netzsch Thermal Analyzers, models STA 449 F1 and Netzsch STA 449 F3. Ar was used as the protective gas and purge gases were O_2 and 1100 ppm O_2 in Ar. Gas flow was controlled by the instrument's internal mass flow controllers, and the total flow rate was either 175 or 180 mL/min. A pressure controller down stream of the TGA outlet was set to maintain a system pressure 3-10 torr above atmospheric pressure to minimize fluctuations caused by changes in atmospheric pressure. The oxygen partial pressure was monitored by a Zirox ZR5 oxygen measuring system that sampled the outlet gas down stream of the pressure controller. Gas mixtures were set such that the pO_2 was $10^{-0.76}$ atm during the oxidation step, and $10^{-3.5}$ or $10^{-4.5}$ atm during the reduction step. Netzsch alumina crucibles were used to hold sample masses were between 300 - 500 mg. Buoyancy effects were removed by subtracting the mass change of a reference sample during identical measurement conditions. Reference samples consisted of crushed Netzsch alumina crucible pieces totaling the same volume as sample measurements. This was calculated using theoretical densities. The mass change during TGA redox experiments for all synthesized materials, including those that successfully exhibited reversible oxygen non-stoichiometry and those that did not, are shown in Supplementary Figure 5 and Supplementary Figure 6, respectively. The mass change for materials that demonstrated reversible oxygen non-stoichiometry was converted to $\Delta\delta$ as described in the main manuscript; these values are also shown in Supplementary Figure 5.

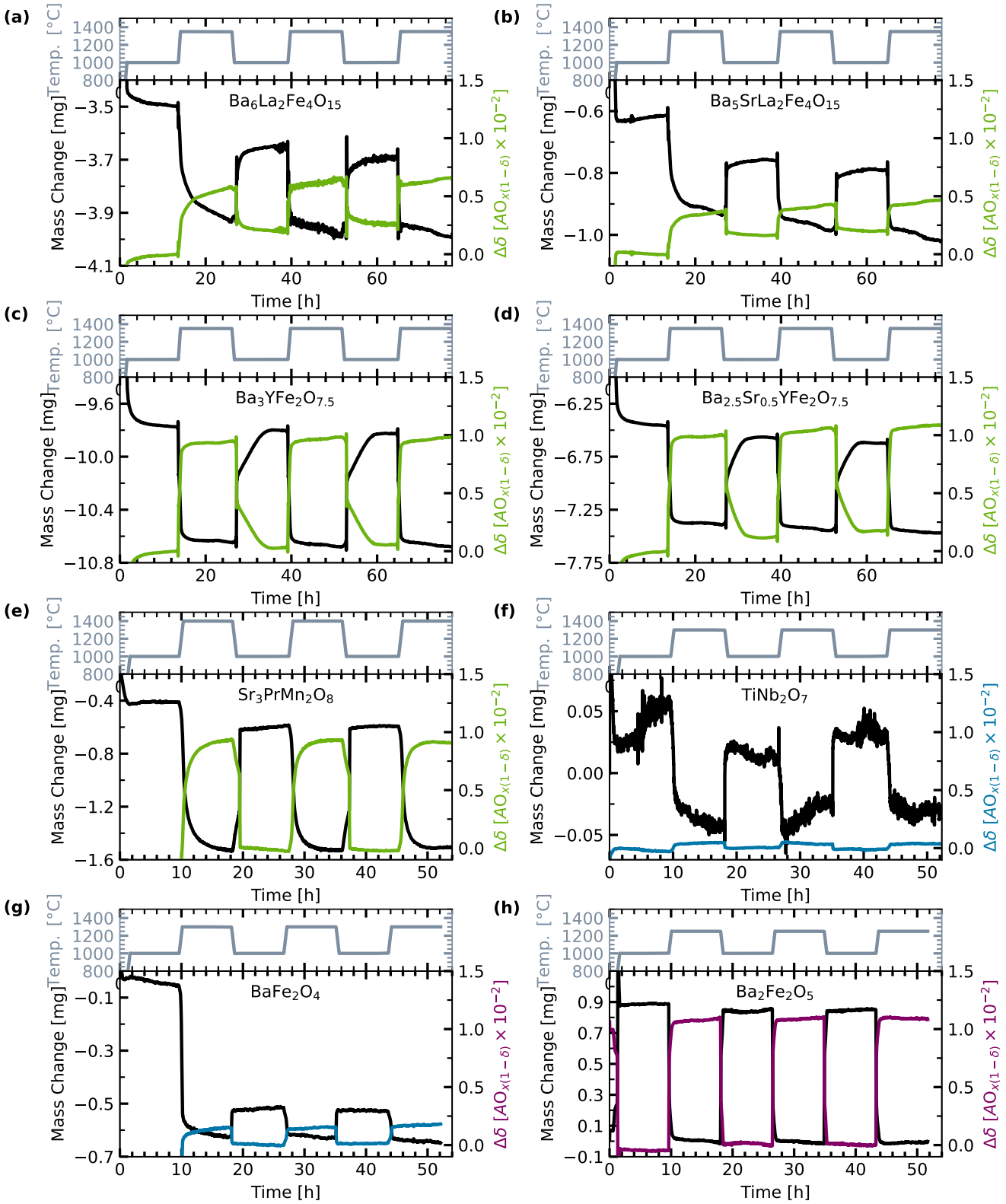

Supplementary Figure 5: Reversible oxygen off-stoichiometry, expressed as $\Delta\delta$ vs. time, in a TGA redox screening experiment for synthesized materials that exhibited reversible mass loss and gain between the second and third cycle.

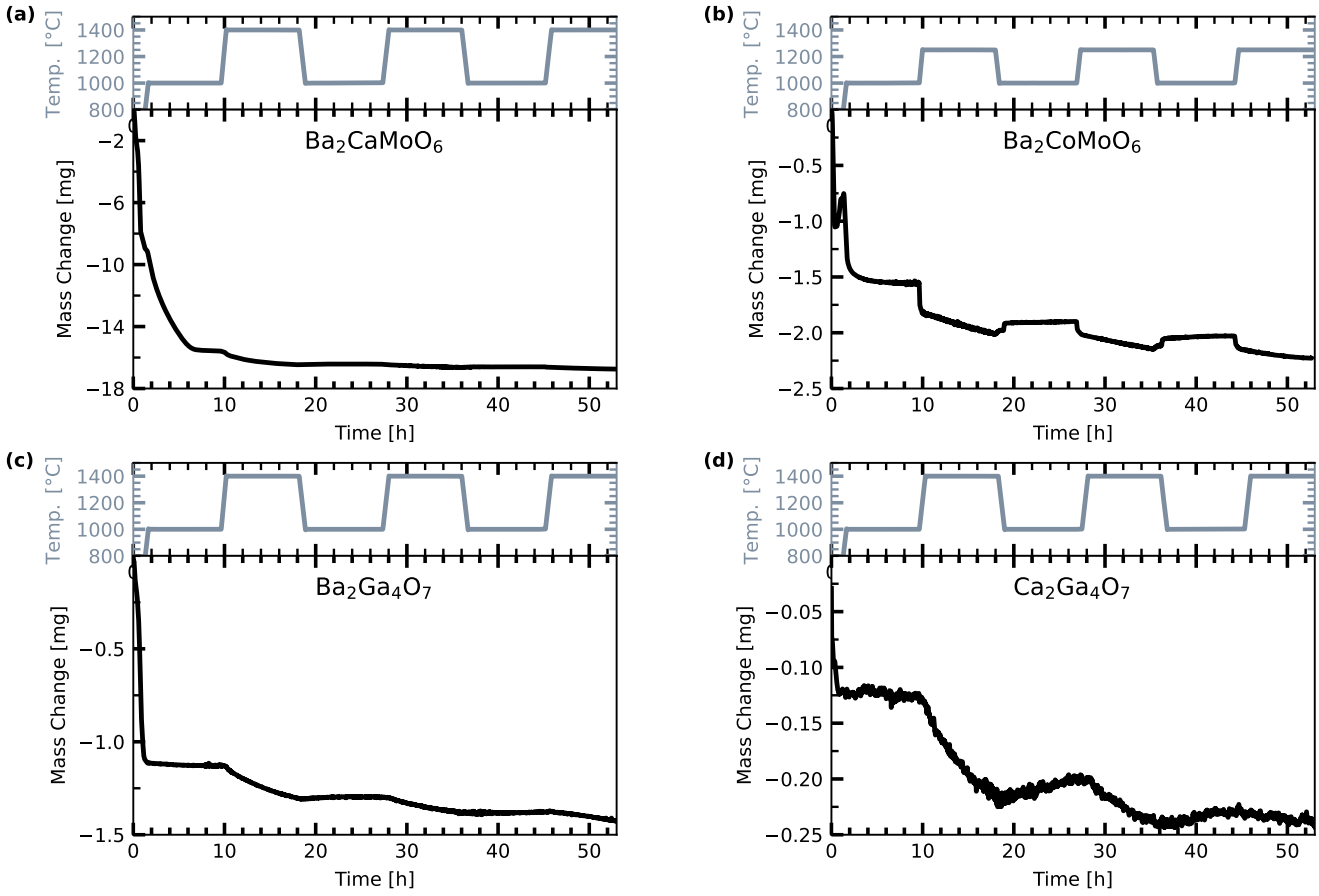

Supplementary Figure 6: Mass loss vs. time in a TGA redox screening experiment for synthesized materials that displayed irreversible mass loss or negligible cycling capacity between the second and third cycle.

Supplementary Section 9. SFR water-splitting cycles

Gas composition is measured downstream of the SFR by a mass spectrometer that is calibrated by flowing aliquots of oxygen and hydrogen through the SFR prepared by mass flow controllers taken from gas mixture standards containing oxygen (25% O_2/Ar) and hydrogen (5% H_2/Ar). The hydrogen production rate, $\dot{n}_{H_2}$, is normalized via

$$\dot{n}_{H_2} = \frac{\dot{Q}_{H_2}}{\nu_{H_2}} \cdot \frac{1}{m_{\text{sample}}} \cdot \frac{M}{N}, \tag{14}$$

where $\dot{Q}_{H_2}$ [cm^3 s^{-1}] is the measured volumetric flow rate from the calibrated mass spectrometer data, $\nu_{H_2} = 22.4$ cm^3 mmol$_{H_2}^{-1}$ is the specific volume of an ideal gas, m_{sample} [g] is the measured sample mass, M [g mol^{-1}] is the molar mass, and N [mol$_{\text{atom}}$ mol^{-1}] is the number of atoms per formula unit. The reactor is supplied with steam from a heated and O_2-depleted water supply through a heated mass flow controller. Gas flow lines are actively heated to prevent steam condensation. Shallow powder beds of ∼0.1 g are subjected to rapid thermochemical cycling under various reduction and oxidation conditions to experimentally assess performance in operational modes of interest for a TCH process. Supplementary Figure 7 shows the SFR water-splitting redox cycle experiments for each material that passed the TGA screening step. H_2 and O_2 production rates are shown for five cycles, and all experimental conditions were identical across all materials tested (see main manuscript) with the exception of T_{red}, which is indicated in the upper temperature profile for each subplot.

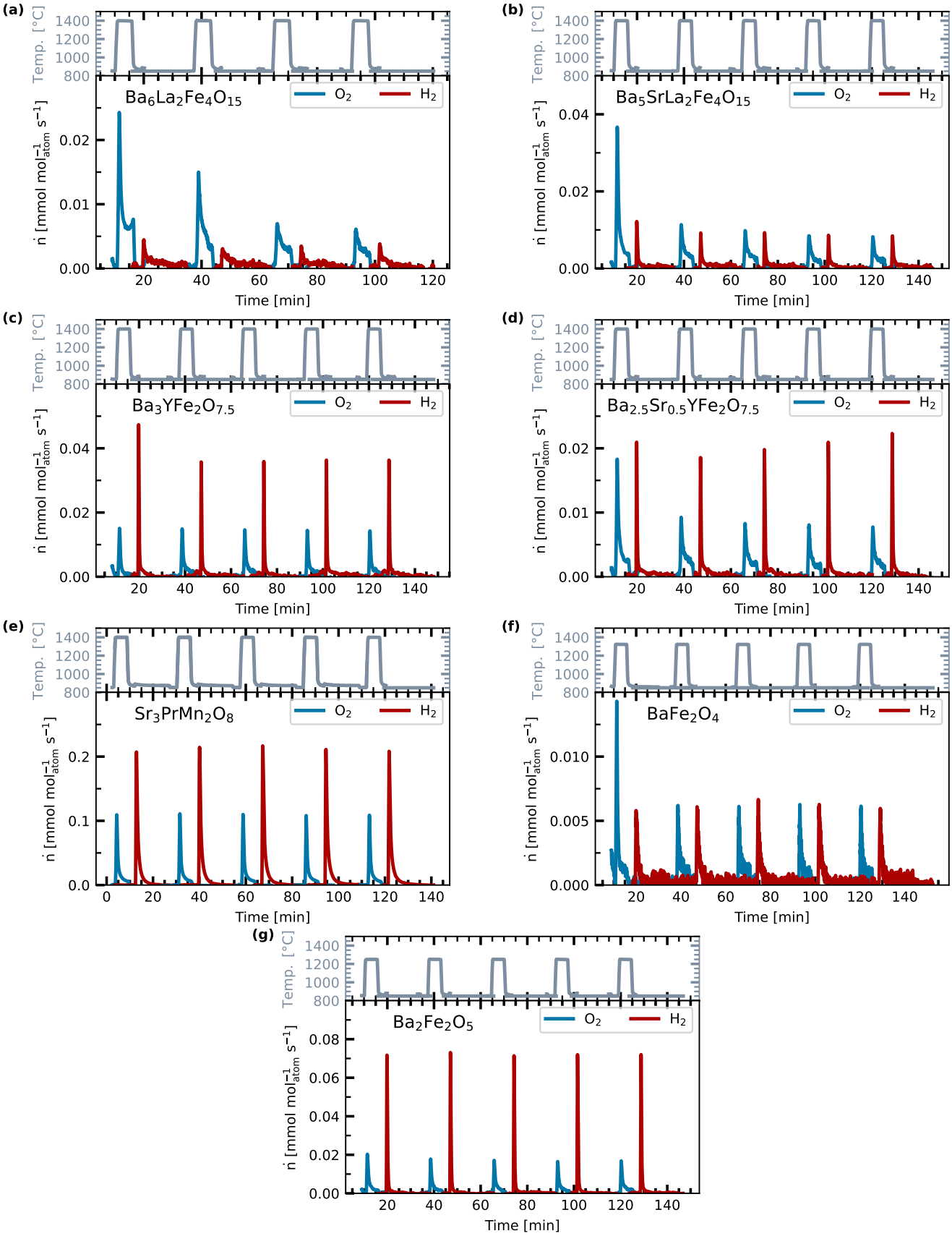

Supplementary Figure 7: SFR experiments showing the H_2 and O_2 production rates for five water-splitting redox cycles for all materials that passed the TGA screening.

References

(1) Hohenberg, P.; Kohn, W. Inhomogeneous electron gas. *Phys. Rev.* **1964**, *136*, B864.

(2) Kohn, W.; Sham, L. J. Self-Consistent Equations Including Exchange and Correlation Effects. *Phys. Rev.* **1965**, *140*, A1133–A1138.

(3) Kresse, G.; Furthmüller, J. Efficient iterative schemes for *ab initio* total-energy calculations using a plane-wave basis set. *Phys. Rev. B* **1996**, *54*, 11169.

(4) Stevanović, V.; Lany, S.; Zhang, X.; Zunger, A. Correcting density functional theory for accurate predictions of compound enthalpies of formation: Fitted elemental-phase reference energies. *Phys. Rev. B* **2012**, *85*, 115104.

(5) Sharan, A.; Lany, S. Computational discovery of stable and metastable ternary oxynitrides. *J. Chem. Phys.* **2021**, *154*, 234706.

(6) Witman, M. D.; Goyal, A.; Ogitsu, T.; McDaniel, A. H.; Lany, S. Defect graph neural networks for materials discovery in high-temperature clean-energy applications. *Nat. Comput. Sci.* **2023**, *3*, 675–686.

(7) Perdew, J. P.; Burke, K.; Ernzerhof, M. Generalized Gradient Approximation Made Simple. *Phys. Rev. Lett.* **1996**, *77*, 3865–3868.

(8) Dudarev, S. L.; Botton, G. A.; Savrasov, S. Y.; Humphreys, C. J.; Sutton, A. P. Electron-energy-loss spectra and the structural stability of nickel oxide: An LSDA+U study. *Phys. Rev. B* **1998**, *57*, 1505–1509.

(9) Blöchl, P. E. Projector augmented-wave method. *Phys. Rev. B* **1994**, *50*, 17953–17979.

(10) Kresse, G.; Joubert, D. From ultrasoft pseudopotentials to the projector augmented-wave method. *Phys. Rev. B* **1999**, *59*, 1758–1775.

(11) Wexler, R. B.; Gautam, G. S.; Stechel, E. B.; Carter, E. A. Factors Governing Oxygen Vacancy Formation in Oxide Perovskites. *J. Am. Chem. Soc.* **2021**, *143*, 13212–13227.

(12) Heyd, J.; Scuseria, G. E.; Ernzerhof, M. Hybrid functionals based on a screened Coulomb potential. *J. Chem. Phys.* **2003**, *118*, 8207–8215.

(13) Heyd, G. E.; Scuseria, J.; Ernzerhof, M. Erratum: "Hybrid functionals based on a screened Coulomb potential"[J. Chem. Phys. 118, 8207 (2003)]. *J. Chem. Phys.* **2006**, *124*, 219906.

(14) Heyd, J.; Scuseria, G. E. Efficient hybrid density functional calculations in solids: Assessment of the Heyd–Scuseria–Ernzerhof screened Coulomb hybrid functional. *J. Chem. Phys.* **2004**, *121*, 1187–1192.

(15) Bahout, M.; Tonus, F.; Prestipino, C.; Pelloquin, D.; Hansen, T.; Fonda, E.; Battle, P. D. High-temperature redox chemistry of $Pr_{0.5}Sr_{1.5}Cr_{0.5}Mn_{0.5}O_{4-\delta}$ investigated in situ by neutron diffraction and X-ray absorption spectroscopy under reducing and oxidizing gas flows. *J. Mater. Chem.* **2012**, *22*, 10560–10570.

(16) Tang, Y.; Cai, Y.; Dou, K.; Chang, J.; Li, W.; Wang, S.; Sun, M.; Huang, B.; Liu, X.; Qiu, J., et al. Dynamic multicolor emissions of multimodal phosphors by Mn^{2+} trace doping in self-activated $CaGa_4O_7$. *Nat. Ccommun.* **2024**, *15*, 3209.

(17) Zhang, J.; Luo, L.; Zhao, W.; Zhang, W.; Hu, Z. Luminescence properties and spectral modulation of the ultra-broadband, highly efficient near-infrared luminescent material $CaGa_4O_7$: Cr^{3+}, Cr^{4+}, Yb^{3+}. *Opt. Mater.* **2023**, *135*, 113388.

(18) Lai, J.; Qiu, J.; Wang, Q.; Zhou, D.; Long, Z.; Yang, Y.; Hu, S.; Li, X.; Pi, J.; Wang, J. Disentangling site occupancy, cation regulation, and oxidation state regulation of the broadband near infrared emission in a chromium-doped $SrGa_4O_7$ phosphor. *Inorg. Chem. Front.* **2020**, *7*, 2313–2321.

(19) Xu, Y.; Luo, L.; Zhao, W.; Zhang, W.; Hu, Z. Highly efficient and stable near-infrared broadband luminescence in SrGa4O7: Cr^{3+}, Yb^{3+} phosphor. *Opt. Mater.* **2023**, *145*, 114460.

(20) Freysoldt, C.; Grabowski, B.; Hickel, T.; Neugebauer, J.; Kresse, G.; Janotti, A.; Van de Walle, C. G. First-principles calculations for point defects in solids. *Rev. Mod. Phys.* **2014**, *86*, 253.

(21) Freysoldt, C.; Neugebauer, J.; Van de Walle, C. G. Fully *ab initio* finite-size corrections for charged-defect supercell calculations. *Phys. Rev. Lett.* **2009**, *102*, 016402.

(22) Freysoldt, C.; Neugebauer, J.; Van de Walle, C. G. Electrostatic interactions between charged defects in supercells. *Phys. Status Solidi B* **2011**, *248*, 1067–1076.

(23) Peng, H.; Scanlon, D. O.; Stevanovic, V.; Vidal, J.; Watson, G. W.; Lany, S. Convergence of density and hybrid functional defect calculations for compound semiconductors. *Phys. Rev. B* **2013**, *88*, 115201.

(24) Behler, J.; Parrinello, M. Generalized neural-network representation of high-dimensional potential-energy surfaces. *Phys. Rev. Lett.* **2007**, *98*, 1–4.

(25) Witman, M.; Goyal, A.; Ogitsu, T.; McDaniel, A. H.; Lany, S. A database of vacancy formation enthalpies for materials discovery (0.0.1) [Data set]. *Zenodo* **2023**, 10.5281/zenodo.8087871.

(26) Witman, M. mwitman1/cgcnndefect: Release for Paper1 (v0.0.0). *Zenodo* **2023**, 10.5281/zenodo.8051401.

(27) Paszke, A. et al. PyTorch: An Imperative Style, High-Performance Deep Learning Library. *Adv. NeurIPS* **2019**, *32*, 8024–8035.

(28) Xie, T.; Grossman, J. C. Crystal Graph Convolutional Neural Networks for an Accurate and Interpretable Prediction of Material Properties. *Phys. Rev. Lett.* **2018**, *120*, 145301.

(29) Zhang, C.; Bengio, S.; Hardt, M.; Recht, B.; Vinyals, O. Understanding Deep Learning (Still) Requires Rethinking Generalization. *Commun. ACM* **2021**, *64*, 107–115.

(30) Stone, K. H.; Cosby, M. R.; Strange, N. A.; Thampy, V.; Walroth, R. C.; Troxel Jr, C. Remote and automated high-throughput powder diffraction measurements enabled by a robotic sample changer at SSRL beamline 2-1. *Journal of Applied Crystallography* **2023**, *56*, 1480–1484.

(31) CrystalMaker-Software-Ltd. CrystalDiffract: a powder diffraction program for Mac and Windows.

(32) Data, M. M. JADE Pro 2024.

(33) Coelho, A. A. TOPAS and TOPAS-Academic: an optimization program integrating computer algebra and crystallographic objects written in C++. *Applied Crystallography* **2018**, *51*, 210–218.

(34) Kabekkodu, S. N.; Dosen, A.; Blanton, T. N. PDF-5+: a comprehensive Powder Diffraction File^{TM} for materials characterization. *Powder Diffraction* **2024**, *39*, 47–59.

(35) Luo, K.; Hayward, M. A. Complex Cation Order in Anion-Deficient $Ba_nYFe_{n-1}O_{2.5n}$ Perovskite Phases. *Inorganic Chemistry* **2012**, *51*, 12281–12287.

(36) R. Barcellos, D.; Sanders, M. D.; Tong, J.; McDaniel, A. H.; O'Hayre, R. P. $BaCe_{0.25}Mn_{0.75}O_{3-\delta}$ - a promising perovskite-type oxide for solar thermochemical hydrogen production. *Energy Environ. Sci.* **2018**, *11*, 3256–3265.

(37) Mevs, H.; Müller-Buschbaum, H. Ba6La2Fe4O15: Ein oxometallat mit neuem strukturtyp. *Journal of the Less Common Metals* **1990**, *157*, 173–178.